iScience

CellPress
OPEN ACCESS

Article

Single-atom catalysts supported on two-dimensional tetragonal transition metal chalcogenides for hydrogen and oxygen evolution

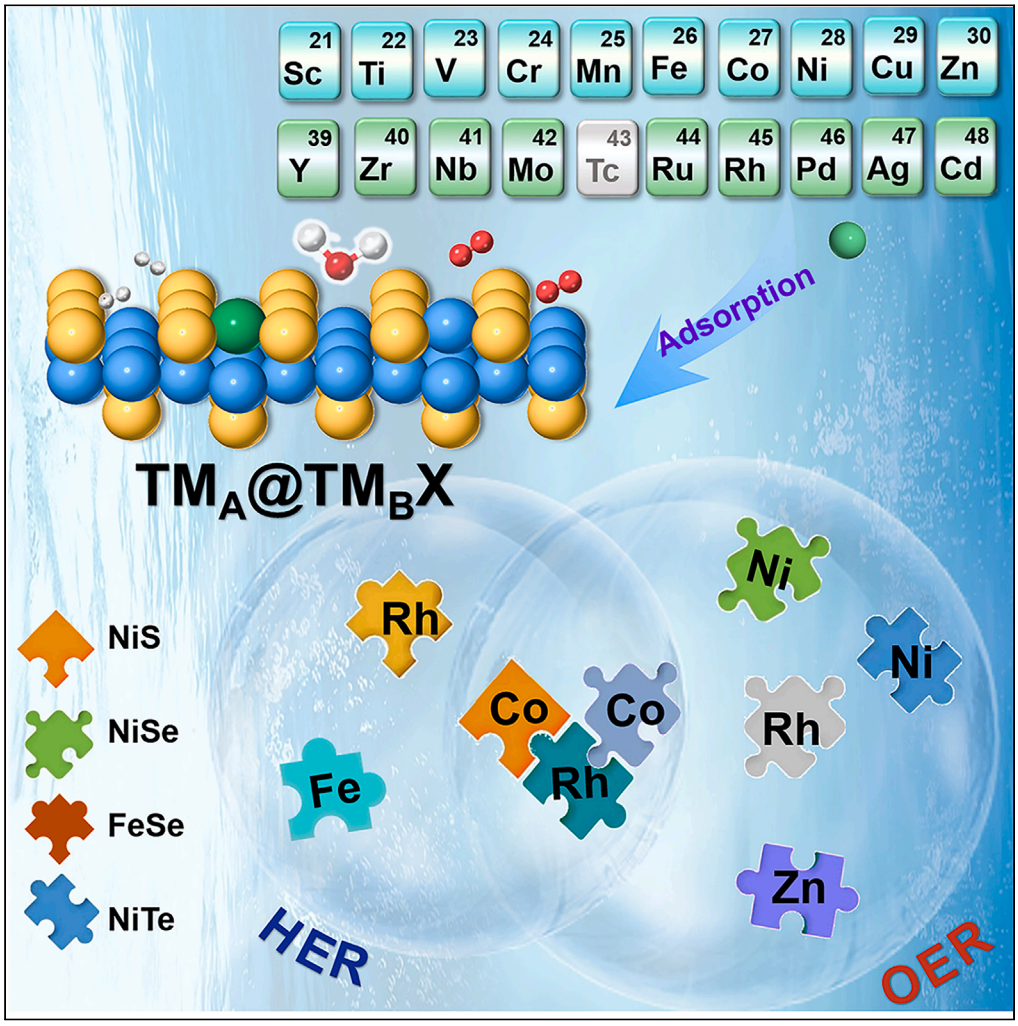

Yumeng Cheng, Jia Zhou

jiazhou@hit.edu.cn

Highlights

TM atoms on 2D TMX are effective in electrocatalytic HER/OER

Three highly active dual functional $TM_A@TM_BX$ for HER/OER are screened out

The d-band center of $TM_A@TM_BX$ with high OER activity is located at a moderate level

Cheng & Zhou, iScience 27, 108788
February 16, 2024
https://doi.org/10.1016/j.isci.2024.108788

iScience

CellPress
OPEN ACCESS

Article

Single-atom catalysts supported on two-dimensional tetragonal transition metal chalcogenides for hydrogen and oxygen evolution

Yumeng Cheng[1] and Jia Zhou[1,2,*]

SUMMARY

Single-atom catalysts (SACs) offer maximum metal atom utilization and high catalytic performance. Transition metal atoms on two-dimensional (2D) materials are effective for improving electrocatalytic performance. However, few studies exist on SACs supported on 2D tetragonal transition metal chalcogenides (TMX) for OER and HER. We report a detailed theoretical study using DFT calculations on SACs supported on TMX monolayers, denoted as $TM_A@TM_BX$. Our findings demonstrate that seven $TM_A@TM_BX$ electrocatalysts surpass IrO_2 (η_{OER} = 0.56 V), with four $TM_A@TM_BX$ exhibiting a reduced OER overpotential compared to RuO_2 (η_{OER} = 0.42 V). Additionally, four $TM_A@TM_BX$ exhibit higher HER performance than Pt (111) (η_{HER} = 0.10 V). We ultimately identified three SACs with high bifunctional HER/OER activity: Co@NiSe, Rh@NiTe, and Co@NiS. This study on $TM_A@TM_BX$ provides insights for enhancing the HER and OER activities of SACs supported on 2D materials, which could have significant implications in clean and renewable energy.

INTRODUCTION

In order to solve the problem of the shortage of non-renewable energy such as fossil fuel and environmental pollution, the research on the development of renewable clean energy is gradually extensive.[1–3] Electrochemical water splitting based on oxygen evolution reaction (OER) and hydrogen evolution reaction (HER) has great potential in clean energy production.[4–6] As a clean, high-energy density, and sustainable secondary energy source, hydrogen produced on the cathode is widely used in fuel supply and material processing. The OER on the anode involves a four-electron transfer process, which is a slow kinetic step that determines the overall rate of the electrocatalytic water splitting reaction.[7,8] The requirement for O_2 in the chemical manufacturing process is consistently increasing, and thus it is imperative to create a new-type and highly effective bifunctional HER and OER electrocatalyst.[9–11] In the past few years, substantial efforts have been made to find less expensive non-precious metal-based electrocatalysts that can match or even surpass the performance of their costlier counterparts.

During recent years, the rapid advancement of material synthesis techniques and characterization methods has led to the growing popularity of single-atom catalysts (SACs) in heterogeneous catalysis. These SACs feature isolated transition metal atoms supported on substrates, which serve as active centers. In comparison to catalysts based on metal clusters or nanoparticles, SACs have a smaller particle size and the distinct local chemical environment of the transition metal atoms which results in higher catalytic performance in various electrocatalytic reactions. Continuous research efforts have been dedicated to the utilization of SACs for electrocatalytic reactions.[12–15] Ali et al. performed a computational study for the mechanism of CO oxidation by O_2 on a single Au atom supported on pristine and nitrogen or boron-doped single-walled carbon nanotubes.[14] It has been discovered that unlike traditional LH and ER mechanisms, oxygen molecules are activated by CO molecules that are pre-adsorbed on Au sites. Yang et al. studied FeS_2-supported transition metal atoms as the electrocatalyst for HER and OER, and found two SACs with excellent bifunctional catalytic performance.[16] Moreover, Chen et al. have theoretically studied single and double transition metal atoms (Co, Cu, Ni, Pt, and Pd) deposited on WS_2 nanosheet as catalyst supports for CO_2 activation and reduction, and found that the Cu- and Co/S-vacancy WS_2 systems were found to have good activity for CO_2 reduction to formic acid and CO.[17] Thus, the catalytic performance of single-atom catalysts has not only been verified under laboratory conditions, but also widely recognized in practical applications. Meanwhile, through theoretical calculations, scientists have successfully revealed the electronic structure and reaction kinetics properties of single-atom catalysts. Single-atom catalysts have become one of the hot research topics in the field of catalysis.

2D tetragonal transition metal chalcogenides TMX (TM = transition metals; X = S, Se, Te) have a unique layered structure and adjustable electronic properties.[18,19] The utilization of TMX as a substrate for SACs could offer a wide range of possibilities for altering the electronic properties of the supported transition metal atoms, thereby optimizing their performance in specific electrocatalytic reactions. Motivated by the outstanding electrocatalytic activity of 2D tetragonal TMX monolayers and the advantages of SACs, it is of great interest to

[1]State Key Laboratory of Urban Water Resource and Environment, School of Science, Harbin Institute of Technology Shenzhen, Shenzhen 518055, China
[2]Lead contact
*Correspondence: jiazhou@hit.edu.cn
https://doi.org/10.1016/j.isci.2024.108788

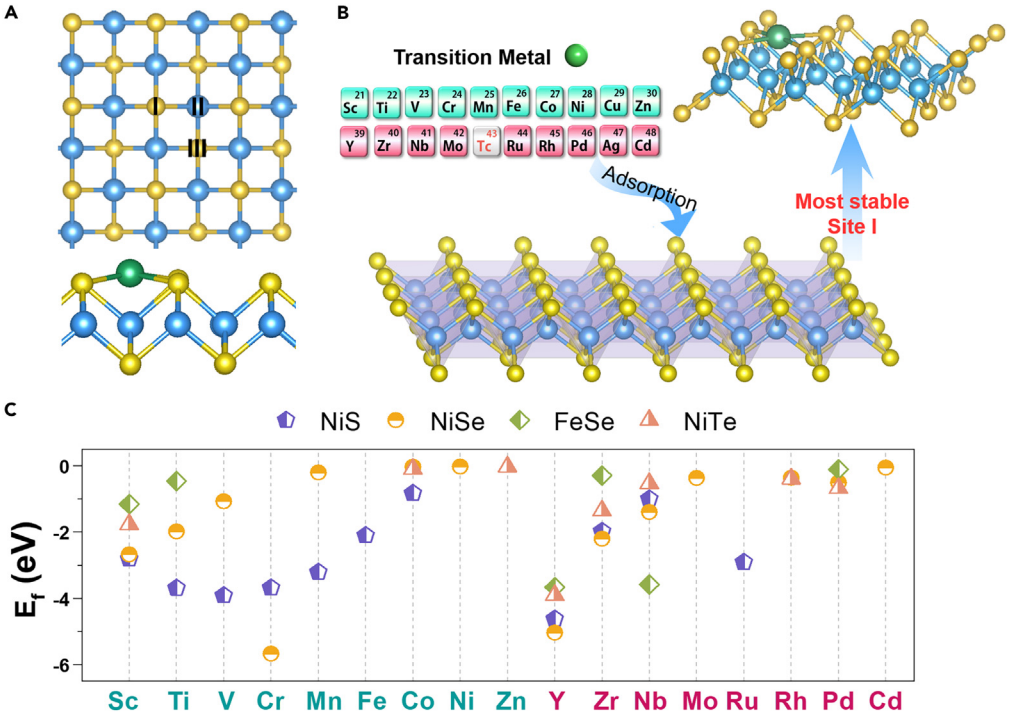

Figure 1. The selection process of TM_A single-atom sites on TM_BX and the stability of TM_A@TM_BX

(A) Three adsorption sites (I-hollow site, II-metal top site, III-nonmetal top site) on TM_BX monolayer.

(B) Schematic diagram of TM atoms adsorption on monolayers to form SACs.

(C) Formation energy of TM_A on four TM_BX monolayers at site I (only show those with negative E_f).

comprehensively investigate the electrochemical performance of transition metal atoms supported on TMX monolayers. By density functional theory (DFT) calculation, we investigated the electrocatalytic water-splitting activities of transition metal single atoms supported on 2D tetragonal transition metal chalcogenides TMX (the SACs denoted as TM_A@TM_BX, and A and B are used to distinguish the two TMs that may be different). The Gibbs free energy change of the adsorbed hydrogen (ΔG_{H^*}) and the OER volcano diagram were used to evaluate the activities of TM_A@TM_BX. At the same time, we used the relationship between the Gibbs free energy of the adsorption intermediates, overpotential, and the *d*-band center to analyze the trend of catalytic activity. Our findings in the current work should provide insight into the role of SACs on TMX monolayers and will be beneficial for the design of other high-performance electrocatalysts.

RESULTS AND DISCUSSION

In our previous work, twenty-two TMX monolayers were found to be thermodynamically stable, and six among them performed well for OER, namely NiSe, NiS, FeSe, CdS, CdSe, and NiTe.[20] Based on the previous results, we chose to investigate the electrocatalytic performance of SACs supported on the aforementioned six TMX monolayers for HER/OER. In order to compare and analyze the performance of SACs (TM_A@TM_BX) and pristine TMX, we labeled all TMX as TM_BX in the discussion section to prevent ambiguity.

Stability screening of SACs

At first, we investigated the stability of a variety of transition metal atoms supported on TM_BX monolayers, so-called TM_A@TM_BX. As shown in Figure 1A, there are three possible sites on the surface of tetragonal TM_BX monolayers that may anchor single metal atoms, namely I (hollow site), II (metal top site), and III (nonmetal top site). The formation energy of TM_A@TM_BX was calculated as:

$$E_f = E_{TMA@TMBX} - E_{TMA} - E_{TMBX} \quad \text{(Equation 1)}$$

where $E_{TMA@TMBX}$, E_{TMBX}, and E_{TMA} are the total energies of the TM_A@TM_BX, TM_BX monolayer, and single TM_A atom in the bulk, respectively. Our calculations revealed that the CdS and CdSe monolayers are unable to stabilize transition metal atoms at all three sites. In addition, for the other four TM_BX monolayers, the formation energy of TM_A atoms at site I is significantly lower than that at site II and III. The formation energy of the TM atom on TM_BX monolayer is inversely proportional to the strength of the chemical adsorption. A more negative formation energy indicates a stronger adsorption, which can prevent the clustering of single atoms on the monolayers and enhance the stability of SACs during electrocatalytic reactions. The stable adsorption of transition metal single atoms on TM_BX monolayers makes it possible to become an

active site in the electrocatalytic reaction. Based on this, we can infer that immobilizing transition metal atoms onto site I of TM_BX is preferable for subsequent HER and OER (Figure 1B). Herein, as shown in Figure 1C, we summarize the results for all $TM_A@TM_BX$ whose formation energies are less than zero, and total count is thirty-nine (the other results are shown in Figure S1A). After metals are loaded onto the TM_BX surface, we observe charge transfer from the metal sites to TM_BX, resulting in positively charged states of the metal sites. It is believed that the positively charged metal sites are closely related to HER/OER intermediates adsorption and reactant activation (Figure S1B).

Electrocatalytic OER/HER performance of SACs

Then, we performed a comprehensive investigation of the catalytic capacity of the thirty-nine SACs. OER is a four-step proton-coupled electron transfer reaction, and the free energy was calculated using Equations 4, 5, 6, and 7. The results are shown in Tables S1–S5. Theoretically, the potential determination step (PDS) is determined by the maximum variation of the four electrochemical steps, as shown in Figure 2A. Upon preliminary screening, we have identified nine SACs with no OER activity, namely Cr@NiS, Y@NiS, Nb@NiSe, Cd@NiSe, Y@NiSe, Y@FeSe, Zr@NiTe, Nb@NiTe, and Y@NiTe. The OER free energy diagrams of the rest thirty $TM_A@TM_BX$ are plotted in Figure 2B. In order to compare the OER performance of SACs more clearly, the PDSs are listed in Figure 2C. It is known that the overpotentials of primitive NiS, NiSe, FeSe, and NiTe monolayers are 1.98, 1.13, 1.16, and 1.21 V, respectively.[18] Notably, the OER performance of all nine $TM_A@NiS$ was found to exhibit better performance than pristine NiS monolayer, highlighting the superiority of SACs. In addition, four kinds of $TM_A@NiSe$ and $TM_A@NiTe$ exhibit excellent OER performance compared to the respective pristine monolayer. For $TM_A@FeSe$, only Pd@FeSe exhibits improved OER performance compared to pristine FeSe. In total, there are eighteen $TM_A@TM_BX$ exhibiting superior OER performance compared to their respective pristine monolayers. Co@NiSe shows the best OER performance with an overpotential of 0.27 V. In addition, the overpotentials of Rh@NiSe (η_{OER} = 0.28 V), Rh@NiTe (η_{OER} = 0.34 V), and Ni@NiTe (η_{OER} = 0.40 V) are also lower than that of than RuO_2 (η_{OER} = 0.42 V).[21] The OER performances of seven SACs outperform IrO_2(110) (η_{OER} = 0.56 V),[7] including Co@NiS, Rh@CoNiSe, Co@NiSe, Ni@NiSe, Rh@NiTe, Ni@NiTe, and Zn@NiTe. These results suggest that the supported transition metal atoms play a crucial role in the improvement of OER activity.

As reported in previous studies, the overpotential of OER is modulated by the adsorption free energy of three oxygenated intermediates (OH*, O*, and OOH*).[22,23] Using the linear relationship between OOH* and OH*, a correlation can be established to give a descriptor to predict and explain OER performance.[24,25] The correlations of the Gibbs free energies of adsorbed OOH* (ΔG_{OOH*}), O* (ΔG_{O*}), and OH* (ΔG_{OH*}) of the eighteen SACs are shown in Figure 3A. The linear relationship between OOH*, O*, and OH* can be expressed by the following equation:

$$\Delta G_{OOH*} = 0.8083\Delta G_{OH*} + 3.1673 \ (R^2 = 0.9633) \quad \text{(Equation 2)}$$

$$\Delta G_{O*} = 1.7501\Delta G_{OH*} + 1.1522 \ (R^2 = 0.9377) \quad \text{(Equation 3)}$$

Based on the strong linear correlation between ΔG_{OH*} and $\Delta G_{OOH*}/\Delta G_{O*}$ in the $TM_A@TM_BX$, it can be inferred that ΔG_{OH*} serves as the independent variable describing the OER overpotential. Accordingly, the colored contour plot and volcano curve were constructed to evaluate the limiting overpotential of SACs, as displayed in Figures 3B and 3C. According to the Sabatier principle,[26] when the adsorption of the intermediate is either too strong or too weak, it will harm the catalytic efficiency of the OER reaction on $TM_A@TM_BX$. An excessive adsorption capacity of the intermediate may hinder its desorption, leading to a decrease in the electrode activity. By contrast, a weak interaction may impede the activation of the reaction intermediate, thereby hindering the promotion of the subsequent reaction. As shown in the Figure 3B, Co@NiSe, Rh@NiSe, Rh@NiTe, Ni@NiTe, Ni@NiSe, Zn@NiTe, and Co@NiS SACs all have an excellent OER performance, and Co@NiSe located at the bottom of the volcano is the best, exhibiting an overpotential of 0.27 V. It also demonstrates that the PDSs of the screened SACs are mainly the second and third steps of the reaction. As shown in Figure 3C, among the screened SACs, there are a total of thirteen SACs with good performance in the enlarged area, and their overpotentials are all less than 1.00 eV. Furthermore, it is worth noting that $TM_A@TM_BX$ SACs in the dark blue region (1.30 eV < $\Delta G_{O*}-\Delta G_{OH*}$ < 1.60 eV) all have a lower overpotential than RuO_2 (η_{OER} = 0.56 V). The detailed OER free energy diagrams of these thirteen $TM_A@TM_BX$ SACs are also summarized in the Figure 3D.

Furthermore, in order to evaluate the HER performances of $TM_A@TM_BX$ SACs, we calculated the Gibbs free energy change (ΔG_{H*}) of H* adsorption. Figure 4A illustrates a schematic representation of H* adsorption on $TM_A@TM_BX$. The Gibbs free energy change ($|\Delta G_{H*}|$) of H* adsorption on the active site, which is considered the most reliable descriptor, directly determines the HER activity of the catalyst. The ideal value of ΔG_{H*} is 0.00 eV, and ΔG_{H*} that deviates too far from zero will inhibit HER activity. In terms of the adsorption intensity, the more positive ΔG_{H*} value indicates that the adsorption kinetics of H* on the catalysts is more difficult. By contrast, the more negative ΔG_{H*} value indicates that H* is easier to be adsorbed on the catalysts, but becomes more difficult to release. Consequently, removing twenty-five kinds of $TM_A@TM_BX$ that cannot effectively adsorb H* at the TM_A site, the ΔG_{H*} of the remaining fourteen $TM_A@TM_BX$ is shown in Figure 4B (see Tables S6 for details). In particular, Rh@NiTe, Fe@NiS, Co@NiS, and Co@NiSe exhibit considerably high HER catalytic activity with their ΔG_{H*} pretty close to zero (−0.006, −0.03, 0.09, and 0.09 eV, respectively). Moreover, Ru@NiS (η_{OER} = 0.11 V) and Rh@NiSe (η_{OER} = 0.11 V) also have the η_{OER} close to precious metal catalyst Pt (0.10 V).[27] We also calculated the theoretical exchange current density i_0, and the i_0 and ΔG_{H*} can be used to quantitatively evaluate the HER performance of the $TM_A@TM_BX$ SACs based on the equation: $i_0 = -ek_0(1+\exp|\Delta G_{H*}|/k_BT)^{-1}$, where k_0 is the rate

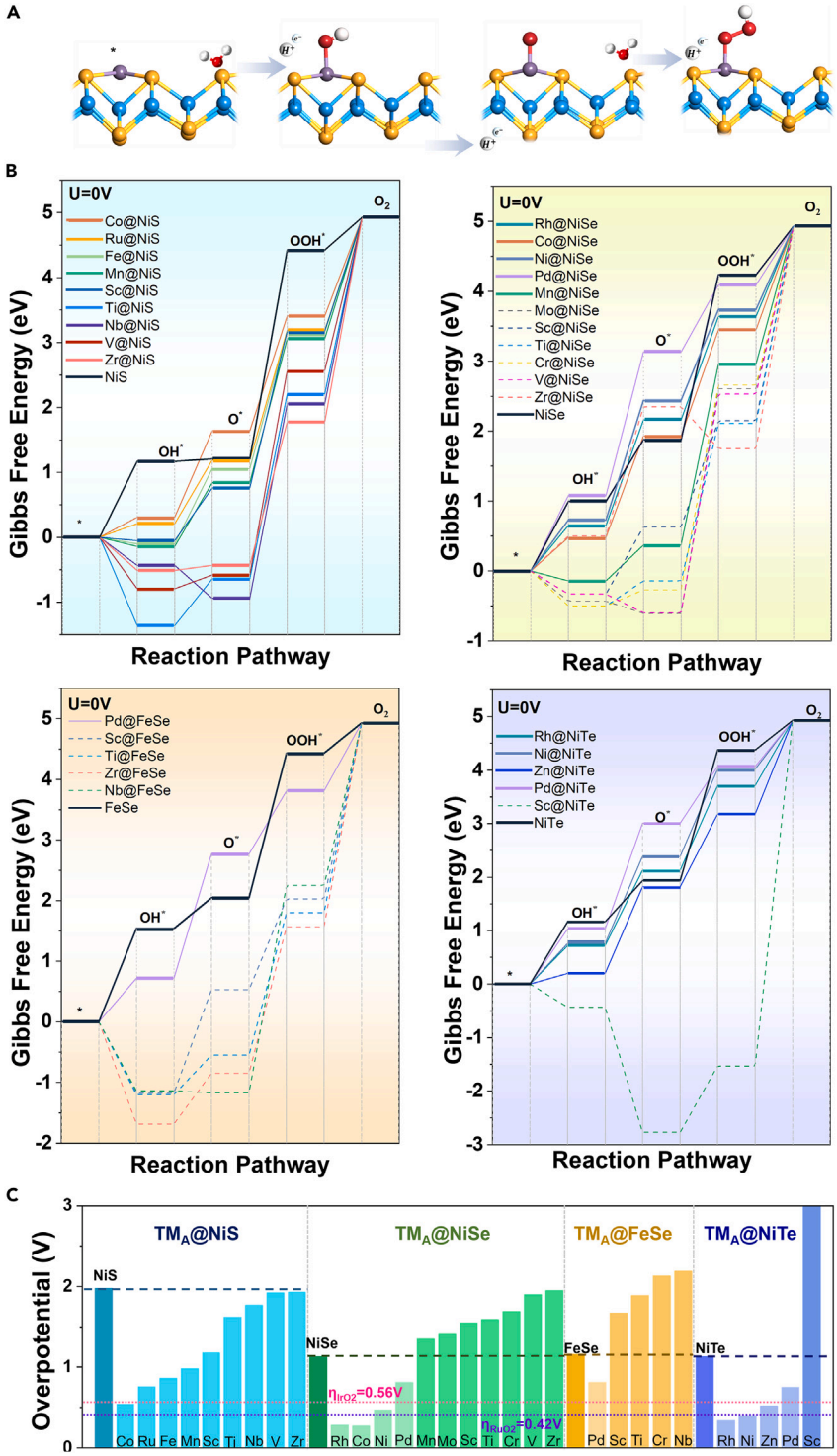

Figure 2. Theoretical calculations of $TM_A@TM_BX$ on the electrocatalytic OER activity

(A) Four-step reaction mechanism of OER by $TM_A@TM_BX$.

(B) OER free energy steps of $TM_A@TM_BX$ (TM_A = transition metals, and TM_BX are NiS, NiSe, NiTe, and FeSe monolayers) under the potential U = 0 V vs. SHE. Solid lines represent the better OER performance of the SACs than the primitive TM_BX monolayers, while dotted lines represent the worse.

(C) OER overpotentials of TM_BX and $TM_A@TM_BX$.

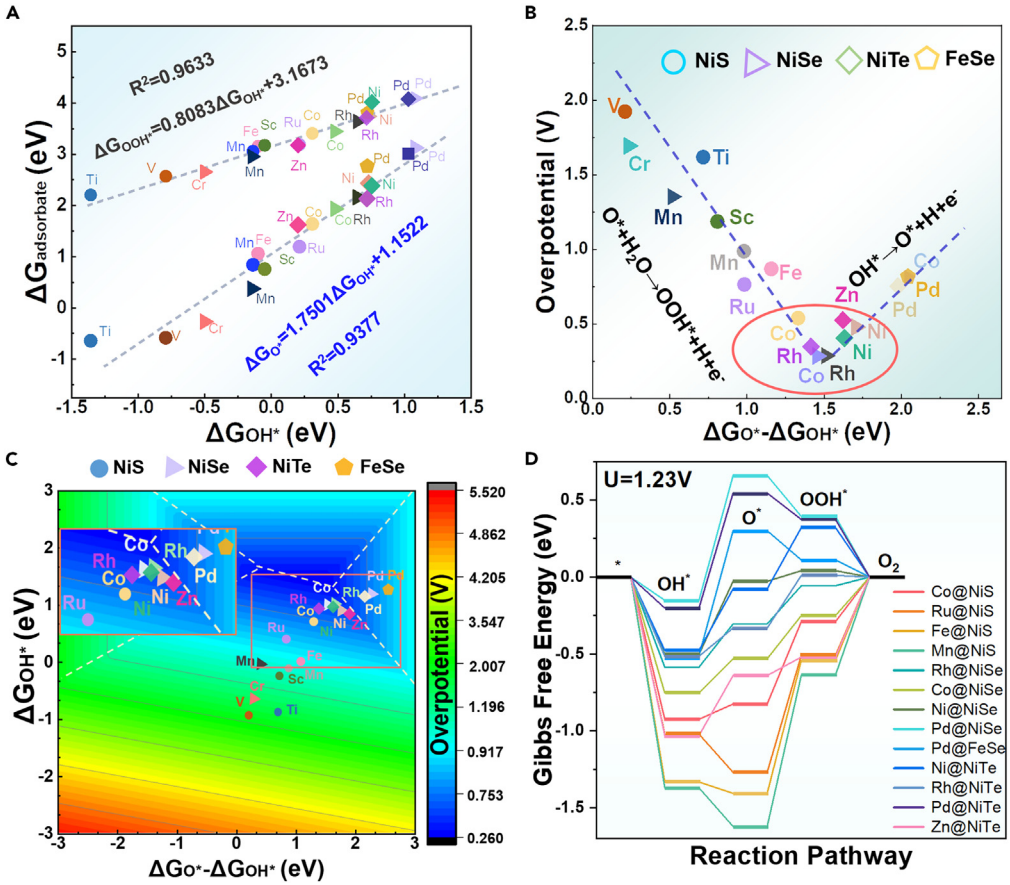

Figure 3. The free energy profile of $TM_A@TM_BX$

(A) The linear relationship for Gibbs free energy of adsorbed OOH*(ΔG_{OOH*}), O*(ΔG_{O*}), and OH* (ΔG_{OH*}).

(B) Volcano curve of OER of the $TM_A@TM_BX$ system, the horizontal axis and the vertical axis are the $\Delta G_{O*}-\Delta G_{OH*}$ and η_{OER}, respectively (The red dotted circle represents catalysts with η_{OER} less than 1.00 V).

(C) The colored OER activity contour plot showing the η as a function of Gibbs free energies of the reaction intermediates.

(D) Free energy diagram for electrocatalysts with OER PDSs less than 1.00 eV at an electrode potential of U = 1.23 V.

constant and k_B is the Boltzmann constant.[28] As shown in Figure 4C, the electrocatalyst at the top of the exchange current volcano has the highest catalytic performance. The electrocatalysts in the enlarged area are close to the "volcano top," and their absolute values of ΔG_{H*} are all less than or close to 0.10 eV. These results demonstrate that Rh@NiTe (η_{HER} = 0.006 V) exhibits the most exceptional i_0 value and is located in the optimal zone (ΔG_{H*} = 0), which indicates its nearly perfect HER catalytic activity. Likewise, Fe@NiS, Co@NiS, and Co@NiSe catalysts are in proximity to the volcanic peak, featuring high exchange current density and low ΔG_{H*}, thereby qualified as commendable HER catalysts. The overpotentials (η_{HER} and η_{OER}) listed previously provide a valuable means to identify bifunctional materials for electrocatalytic reactions. As shown in Figure 5 and Table S7, Co@NiSe, Rh@NiTe, and Co@NiS exhibit low η_{HER}/η_{OER} values of 0.09/0.27, 0.006/0.34, and 0.09/0.53 V, respectively, and can therefore serve as effective and efficient HER/OER bifunctional SACs, having high practical potential in the overall water splitting.

Origins of electrocatalytic OER of SACs

Despite the identification of catalysts with high performance through the aforementioned calculations, it is imperative to gain further insight into the correlation between the catalyst's structure and its activity to facilitate the design of more efficient SACs. Given the higher OER overpotential of most SACs compared to HER, as depicted in Figure 5, and the limited descriptors available for HER activity, in this part, our investigation focused on exploring the relationship between OER activity and intrinsic characteristics to guide the design of more efficient SACs. The *d*-band center theory has been good at revealing the origin of catalysis activity.[26] Partial density of states of *d*-orbitals for thirteen $TM_A@TM_BX$ with overpotential below 1.00 eV are shown in Figure 6A, and *d*-band centers of $TM_A@TM_BX$ are listed in Table S8. According to the *d*-band center theory and Sabatier's principle, the closer the d-band center (ε_d) is to the Fermi level usually indicates stronger adsorption interaction between the substrate and the adsorbates, which is more beneficial to the catalytic reaction process.[29] We found in previous studies that a moderate *d*-band center will maximize catalytic activity.[30–32] The relationships between ΔG (OH*, O*, and OOH*) and ε_d were

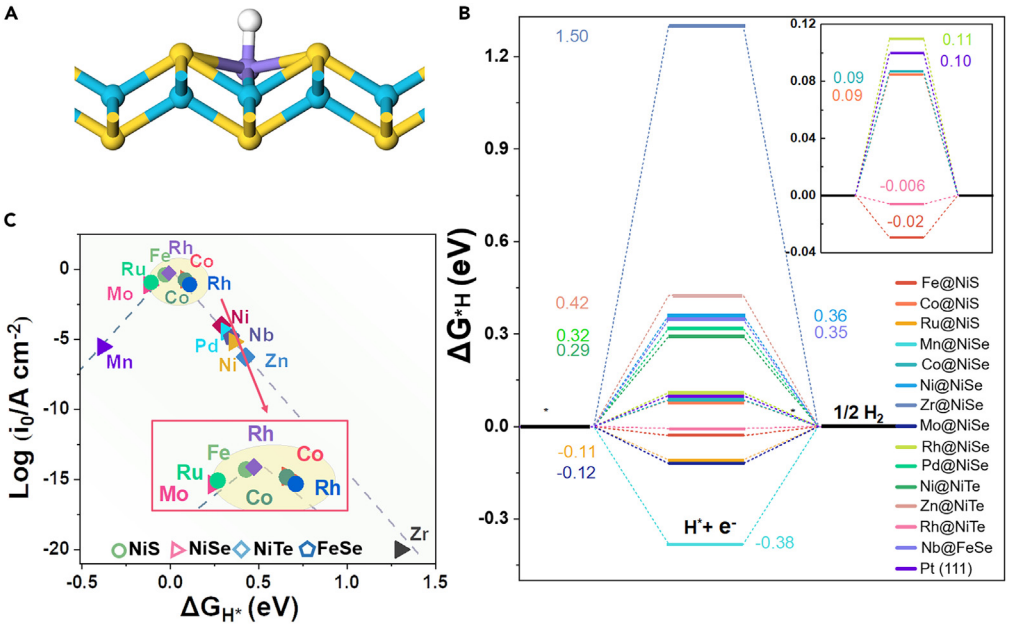

Figure 4. Theoretical calculations of $TM_A@TM_BX$ on the electrocatalytic HER activity

(A) Schematic representation of H* adsorption on $TM_A@TM_BX$.

(B) HER performances of fourteen $TM_A@TM_BX$. The inset shows potential electrocatalysts within the criterion $|\Delta G_{H^*}| < 0.11$ eV.

(C) HER volcano curve of the exchange current (i_0) of $TM_A@TM_BX$ with ΔG_{H^*} varying from −0.50 to 1.50 eV.

shown in Figure 6B. It can be clearly observed that the *d*-band center of SACs with high OER activity is moderate and will not be too far or too close to the Fermi level (the circled part in the Figure 6B). These SACs with intermediates of moderate adsorption exhibit excellent catalytic activity during the OER reaction process. Therefore, appropriate adsorption and desorption capabilities of reaction intermediates, as well as high charge density and fast electron transfer efficiency of active centers, can significantly improve electrocatalytic activity, as stated in previous study.[33] In order to better understand that a moderate *d*-band center is most advantageous for catalytic processes, we also investigated the relationship between the overpotentials and *d*-centers of these thirteen catalysts, as shown in Figure 6C. Compared with the respective TM_BX monolayer, it is worth noting that the supported TM_A often exhibits the improved catalytic activity when it has a moderate *d*-band center. Taking $TM_A@NiSe$ as an example (Mn@NiSe was added in Figure 6C for better analysis), the *d*-band center of the TM_A in Mn@NiSe,

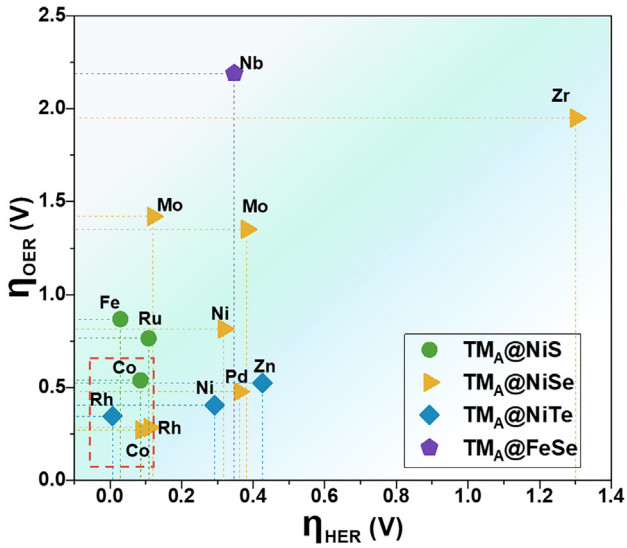

Figure 5. Computational screening of $TM_A@TM_BX$ SACs based on η_{OER} vs. η_{HER} plots

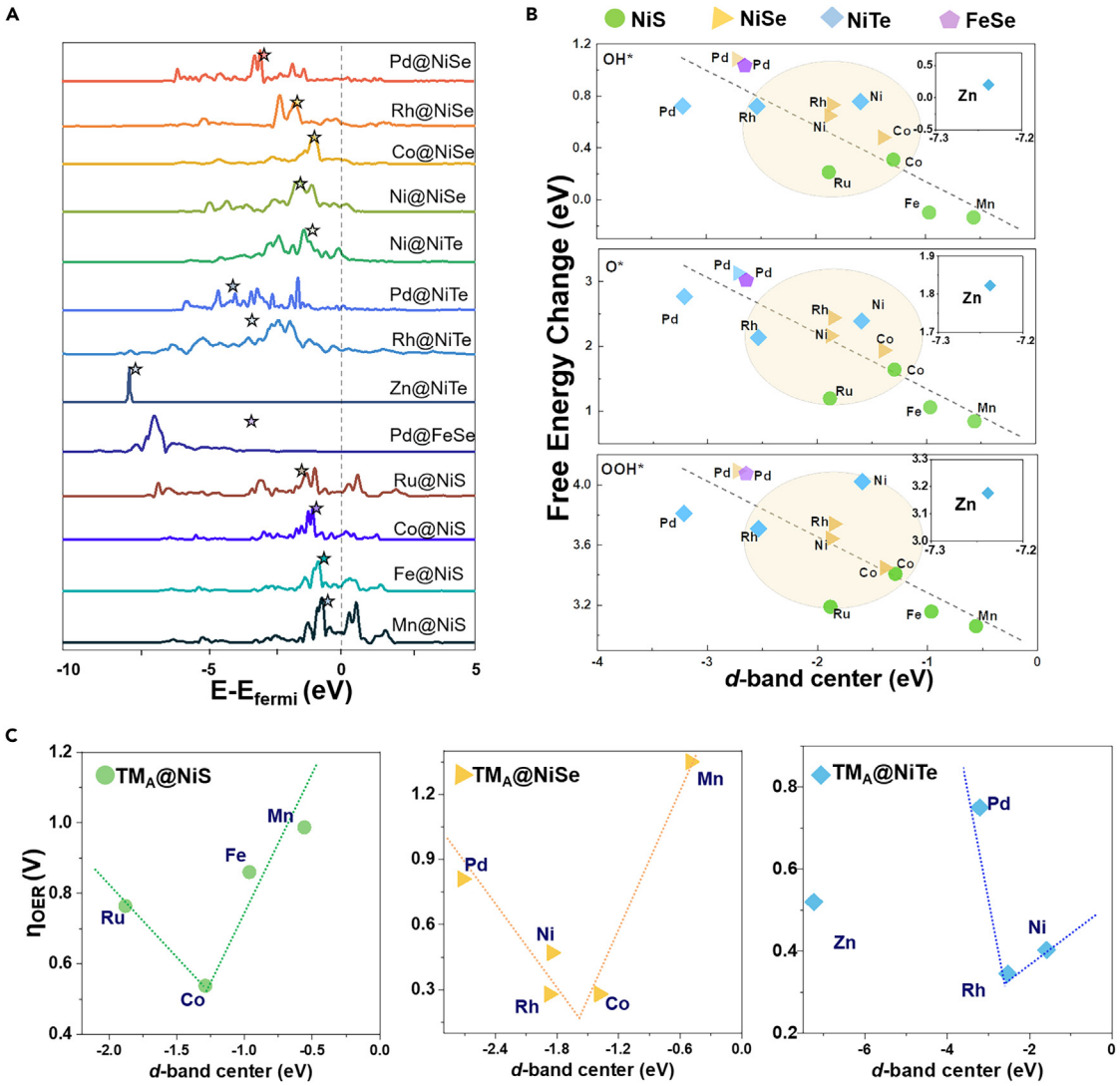

Figure 6. The correlation between the d-band center and OER adsorption energy of intermediates and overpotential

(A) PDOS of *d* orbitals for $TM_A@TM_BX$.

(B) Relationships between OH*, OOH*, and O* Gibbs free energy and the *d*-band center.

(C) Relationships between η_{OER} and *d*-band center.

Pd@NiSe, Ni@NiSe, Co@NiSe, and Rh@NiSe is in the order of Pd (−2.72 eV) < Ni (−1.87 eV) < Co (−1.85 eV) < Rh (−1.38 eV) < Mn (−0.51 eV) relative to the Fermi energy level. Co@NiSe (η_{OER} = 0.27 V) and Rh@NiSe (η_{OER} = 0.28 V) at the middle level in the center of the *d*-band have lower overpotentials than the other three. The aforementioned findings are further corroborated by the electrochemical performance of $TM_A@NiTe$ and $TM_A@NiS$ catalysts, which exhibit similar trends (Zn@NiTe is not taken into consideration due to its significant deviation). It is worth noting that the TM_A of the thirteen SACs with better activity are from the VIII group of the periodic table. TM_BX-supported Co and Rh SACs demonstrate the most outstanding catalytic activity. Meanwhile, Co@NiS and Co@NiSe exhibit OER activity superior to that of Ru@NiS, Pd@NiSe, and Rh@NiSe. Single-atom catalysts with Co as the active center have shown excellent performance in previous electrocatalytic reaction studies, and both experiments and calculations have shown that Co exhibits excellent activity in catalysts through synergistic metal-support interactions.[34–36] This is further evidence of the potential of non-precious metal Co as an alternative to precious metals such as Pd, Ru, and Rh.

Conclusion

In summary, we systematically investigated the OER and HER electrocatalytic activity of single-atom catalysts supported on 2D tetragonal transition metal chalcogenide monolayers by using DFT calculations. Among the thirty-nine stable SACs, we have found that there are four $TM_A@TM_BX$ with OER performance superior to RuO_2, seven SACs with OER performance superior to IrO_2, and four SACs with HER

performance superior to Pt. Notably, Co@NiSe displays the best OER performance (η_{OER} = 0.27 V), followed by Rh@NiSe and Rh@NiTe. Moreover, Rh@NiTe exhibits highly efficient HER catalytic activity with remarkably low overpotentials (0.006 V). Overall, Co@NiSe, Rh@NiTe, and Co@NiS exhibit exceptional bifunctional catalytic activity for both OER and HER. These results offer valuable insights into the optimization of bifunctional electrocatalysts for HER and OER activities, thereby paving the way for the further development of high-performance SACs.

Limitations of the study

Our work demonstrates the high activity of single-atom catalysts supported on TMX for HER/OER by DFT calculations, and explains their activity using descriptors. However, the impact of different TMX on activity still needs to be explored, which will also be our future research.

STAR★METHODS

Detailed methods are provided in the online version of this paper and include the following:

- KEY RESOURCES TABLE
- RESOURCE AVAILABILITY
  - Lead contact
  - Materials availability
  - Data and code availability
- METHOD DETAILS
- QUANTIFICATION AND STATISTICAL ANALYSIS

SUPPLEMENTAL INFORMATION

Supplemental information can be found online at https://doi.org/10.1016/j.isci.2024.108788.

ACKNOWLEDGMENTS

This work was supported by State Key Laboratory of Urban Water Resource and Environment (Harbin Institute of Technology) (No. 2022TS36) and Natural Science Foundation of Guangdong Province (No. 2023A1515011332).

AUTHOR CONTRIBUTIONS

All calculations, analyses, manuscript writing, and revisions in the manuscript were completed by Y.C. and J.Z.

DECLARATION OF INTERESTS

The authors declare no competing interests.

Received: August 20, 2023
Revised: September 28, 2023
Accepted: January 2, 2024
Published: January 4, 2024

REFERENCES

1. Greeley, J., and Markovic, N.M. (2012). The road from animal electricity to green energy: combining experiment and theory in electrocatalysis. Energy Environ. Sci. *5*, 9246–9256.
2. Seh, Z.W., Kibsgaard, J., Dickens, C.F., Chorkendorff, I.B., Nørskov, J.K., and Jaramillo, T.F. (2017). Combining theory and experiment in electrocatalysis: Insights into materials design. Science *355*, eaad4998.
3. Yang, Z., Zhang, J., Kintner-Meyer, M.C.W., Lu, X., Choi, D., Lemmon, J.P., and Liu, J. (2011). Electrochemical Energy Storage for Green Grid. Chem. Rev. *111*, 3577–3613.
4. Gray, H.B. (2009). Powering the planet with solar fuel. Nat. Chem. *1*, 112.
5. Guo, M., Wang, L., Zhan, J., Jiao, X., Chen, D., and Wang, T. (2020). A novel design of an electrolyser using a trifunctional (HER/OER/ORR) electrocatalyst for decoupled H_2/O_2 generation and solar to hydrogen conversion. J. Mater. Chem. A *8*, 16609–16615.
6. Zhang, K., and Zou, R. (2021). Advanced Transition Metal-Based OER Electrocatalysts: Current Status, Opportunities, and Challenges. Small *17*, 2100129.
7. Man, I.C., Su, H.Y., Calle-Vallejo, F., Hansen, H.A., Martínez, J.I., Inoglu, N.G., Kitchin, J., Jaramillo, T.F., Nørskov, J.K., and Rossmeisl, J. (2011). Universality in Oxygen Evolution Electrocatalysis on Oxide Surfaces. ChemCatChem *3*, 1159–1165.
8. Wei, C., Rao, R.R., Peng, J., Huang, B., Stephens, I.E.L., Risch, M., Xu, Z.J., and Shao-Horn, Y. (2019). Recommended Practices and Benchmark Activity for Hydrogen and Oxygen Electrocatalysis in Water Splitting and Fuel Cells. Adv. Mater. *31*, 1806296.
9. Jiao, Y., Zheng, Y., Jaroniec, M., and Qiao, S.Z. (2015). Design of electrocatalysts for oxygen- and hydrogen-involving energy conversion reactions. Chem. Soc. Rev. *44*, 2060–2086.
10. Li, Y., Wang, H., Xie, L., Liang, Y., Hong, G., and Dai, H. (2011). MoS2 Nanoparticles Grown on Graphene: An Advanced Catalyst for the Hydrogen Evolution Reaction. J. Am. Chem. Soc. *133*, 7296–7299.
11. Wang, J., Xu, F., Jin, H., Chen, Y., and Wang, Y. (2017). Non-Noble Metal-based Carbon Composites in Hydrogen Evolution Reaction: Fundamentals to Applications. Adv. Mater. *29*, 1605838.
12. Yasin, G., Ali, S., Ibraheem, S., Kumar, A., Tabish, M., Mushtaq, M.A., Ajmal, S., Arif, M., Khan, M.A., Saad, A., et al. (2023). Simultaneously Engineering the Synergistic-Effects and Coordination-Environment of

Dual-Single-Atomic Iron/Cobalt-sites as a Bifunctional Oxygen Electrocatalyst for Rechargeable Zinc-Air Batteries. ACS Catal. *13*, 2313–2325.

13. Ali, S., Liu, T., Lian, Z., Sheng Su, D., and Li, B. (2019). The stability and reactivity of transition metal atoms supported mono and di vacancies defected carbon based materials revealed from first principles study. Appl. Surf. Sci. *473*, 777–784.
14. Ali, S., Liu, T., Lian, Z., Li, B., and Su, D.S. (2017). The tunable effect of nitrogen and boron dopants on a single walled carbon nanotube support on the catalytic properties of a single gold atom catalyst: a first principles study of CO oxidation. J. Mater. Chem. A *5*, 16653–16662.
15. Ibraheem, S., Yasin, G., Kumar, A., Mushtaq, M.A., Ibrahim, S., Iqbal, R., Tabish, M., Ali, S., and Saad, A. (2022). Iron-cation-coordinated cobalt-bridged-selenides nanorods for highly efficient photo/electrochemical water splitting. Appl. Catal. B Environ. *304*, 120987.
16. Yang, Y., Liu, J., Liu, F., Wang, Z., and Wu, D. (2021). FeS_2-anchored transition metal single atoms for highly efficient overall water splitting: a DFT computational screening study. J. Mater. Chem. A *9*, 2438–2447.
17. Ismail, P.M., Ali, S., Raziq, F., Bououdina, M., Abu-Farsakh, H., Xia, P., Wu, X., Xiao, H., Ali, S., and Qiao, L. (2023). Stable and robust single transition metal atom catalyst for CO_2 reduction supported on defective WS_2. Appl. Surf. Sci. *624*, 157073.
18. Zhou, J., Cheng, Y., and Zhu, Y. (2022). Theoretical study of two-dimensional tetragonal transition metal chalcogenides and the potassium derivatives. Sustain. Energy Fuels *6*, 1770–1779.
19. Zhou, J., Cheng, Y., and Zhu, Y. (2022). Survey of Tetragonal Transition Metal Chalcogenide Hetero-Bilayers for Promising Photocatalysts. Adv. Mater. Interfac. *9*, 2102334.
20. Cheng, Y., and Zhou, J. (2023). Two-Dimensional Tetragonal Transition Metal Chalcogenides for High Performance Oxygen Evolution and Reduction: A DFT Study (ChemPhysChem *n/a*), p. e202300714.
21. Lee, Y., Suntivich, J., May, K.J., Perry, E.E., and Shao-Horn, Y. (2012). Synthesis and Activities of Rutile IrO_2 and RuO_2 Nanoparticles for Oxygen Evolution in Acid and Alkaline Solutions. J. Phys. Chem. Lett. *3*, 399–404.
22. Jakub, Z., Kraushofer, F., Bichler, M., Balajka, J., Hulva, J., Pavelec, J., Sokolović, I., Müllner, M., Setvin, M., Schmid, M., et al. (2019). Partially Dissociated Water Dimers at the Water-Hematite Interface. ACS Energy Lett. *4*, 390–396.
23. Reda, M., Hansen, H.A., and Vegge, T. (2018). DFT Study of the Oxygen Reduction Reaction on Carbon-Coated Iron and Iron Carbide. ACS Catal. *8*, 10521–10529.
24. Kan, D., Lian, R., Wang, D., Zhang, X., Xu, J., Gao, X., Yu, Y., Chen, G., and Wei, Y. (2020). Screening effective single-atom ORR and OER electrocatalysts from Pt decorated MXenes by first-principles calculations. J. Mater. Chem. A *8*, 17065–17077.
25. Li, M., Zhang, L., Xu, Q., Niu, J., and Xia, Z. (2014). N-doped graphene as catalysts for oxygen reduction and oxygen evolution reactions: Theoretical considerations. J. Catal. *314*, 66–72.
26. Ling, C., Shi, L., Ouyang, Y., Zeng, X.C., and Wang, J. (2017). Nanosheet Supported Single-Metal Atom Bifunctional Catalyst for Overall Water Splitting. Nano Lett. *17*, 5133–5139.
27. Xu, H., Cheng, D., Cao, D., and Zeng, X.C. (2018). A universal principle for a rational design of single-atom electrocatalysts. Nat. Catal. *1*, 339–348.
28. Nørskov, J.K., Bligaard, T., Logadottir, A., Kitchin, J.R., Chen, J.G., Pandelov, S., and Stimming, U. (2005). Trends in the exchange current for hydrogen evolution. J. Electrochem. Soc. *152*, J23–J26.
29. Medford, A.J., Vojvodic, A., Hummelshøj, J.S., Voss, J., Abild-Pedersen, F., Studt, F., Bligaard, T., Nilsson, A., and Nørskov, J.K. (2015). From the Sabatier principle to a predictive theory of transition-metal heterogeneous catalysis. J. Catal. *328*, 36–42.
30. Fu, Z., Ling, C., and Wang, J. (2020). A $Ti_3C_2O_2$ supported single atom, trifunctional catalyst for electrochemical reactions. J. Mater. Chem. A *8*, 7801–7807.
31. Niu, H., Wan, X., Wang, X., Shao, C., Robertson, J., Zhang, Z., and Guo, Y. (2021). Single-Atom Rhodium on Defective g-C_3N_4: A Promising Bifunctional Oxygen Electrocatalyst. ACS Sustain. Chem. Eng. *9*, 3590–3599.
32. Liu, X., Liu, T., Xiao, W., Wang, W., Zhang, Y., Wang, G., Luo, Z., and Liu, J.-C. (2022). Strain engineering in single-atom catalysts: $GaPS_4$ for bifunctional oxygen reduction and evolution. Inorg. Chem. Front. *9*, 4272–4280.
33. Zhang, S., Xue, H., Li, W.-l., Sun, J., Guo, N., Song, T., Dong, H., Zhang, J., Ge, X., Zhang, W., and Wang, Q. (2021). Constructing Precise Coordination of Nickel Active Sites on Hierarchical Porous Carbon Framework for Superior Oxygen Reduction. Small *17*, 2102125.
34. Li, L., Liu, X., Wang, J., Liu, R., Liu, Y., Wang, C., Yang, W., Feng, X., and Wang, B. (2022). Atomically dispersed Co in a cross-channel hierarchical carbon-based electrocatalyst for high-performance oxygen reduction in Zn-air batteries. J. Mater. Chem. A *10*, 18723–18729.
35. Li, Z., Leng, L., Ji, S., Zhang, M., Liu, H., Gao, J., Zhang, J., Horton, J.H., Xu, Q., and Zhu, J. (2022). Engineering the morphology and electronic structure of atomic cobalt-nitrogen-carbon catalyst with highly accessible active sites for enhanced oxygen reduction. J. Energy Chem. *73*, 469–477.
36. Kumar, P., Kannimuthu, K., Zeraati, A.S., Roy, S., Wang, X., Wang, X., Samanta, S., Miller, K.A., Molina, M., Trivedi, D., et al. (2023). High-Density Cobalt Single-Atom Catalysts for Enhanced Oxygen Evolution Reaction. J. Am. Chem. Soc. *145*, 8052–8063.
37. Kresse, G., and Furthmüller, J. (1996). Efficiency of ab-initio total energy calculations for metals and semiconductors using a plane-wave basis set. Comput. Mater. Sci. *6*, 15–50.
38. Kresse, G., and Hafner, J. (1994). Ab-initio Molecular-dynamics Simulation of the Liquid-metal amorphous-semiconductor Transition in Germanium. Phys. Rev. B *49*, 14251–14269.
39. Blöchl, P. (1994). Projector Augmented-Wave MEthod. Phys. Rev. B *50*, 17953–17979.
40. Perdew, J.P., Burke, K., and Ernzerhof, M. (1996). Generalized gradient approximation made simple. Phys. Rev. Lett. *77*, 3865–3868.
41. Grimme, S., Antony, J., Ehrlich, S., and Krieg, H. (2010). A consistent and accurate ab initio parametrization of density functional dispersion correction (DFT-D) for the 94 elements H-Pu. J. Chem. Phys. *132*, 154104.
42. Pack, J.D., and Monkhorst, H.J. (1977). Special points for brillouin-zone integrations - reply. Phys. Rev. B *16*, 1748–1749.
43. Mathew, K., Sundararaman, R., Letchworth-Weaver, K., Arias, T.A., and Hennig, R.G. (2014). Implicit solvation model for density-functional study of nanocrystal surfaces and reaction pathways. J. Chem. Phys. *140*, 084106.
44. Nørskov, J.K., Rossmeisl, J., Logadottir, A., Lindqvist, L., Kitchin, J.R., Bligaard, T., and Jónsson, H. (2004). Origin of the overpotential for oxygen reduction at a fuel-cell cathode. J. Phys. Chem. B *108*, 17886–17892.
45. Gao, G., Bottle, S., and Du, A. (2018). Understanding the activity and selectivity of single atom catalysts for hydrogen and oxygen evolution via ab initial study. Catal. Sci. Technol. *8*, 996–1001.
46. Nørskov, J.K., Abild-Pedersen, F., Studt, F., and Bligaard, T. (2011). Density functional theory in surface chemistry and catalysis. Proc. Natl. Acad. Sci. USA *108*, 937–943.
47. Lozovoi, A.Y., and Alavi, A. (2003). Reconstruction of charged surfaces: General trends and a case study of Pt(110) and Au(110). Phys. Rev. B *68*, 245416.
48. Lozovoi, A.Y., Alavi, A., Kohanoff, J., and Lynden-Bell, R.M. (2001). Ab initio simulation of charged slabs at constant chemical potential. J. Chem. Phys. *115*, 1661–1669.
49. Tan, S., Ji, Y., and Li, Y. (2022). Single-Atom Electrocatalysis for Hydrogen Evolution Based on the Constant Charge and Constant Potential Models. J. Phys. Chem. Lett. *13*, 7036–7042.
50. Ha, M., Kim, D.Y., Umer, M., Gladkikh, V., Myung, C.W., and Kim, K.S. (2021). Tuning metal single atoms embedded in NxCy moieties toward high-performance electrocatalysis. Energy Environ. Sci. *14*, 3455–3468.
51. Huang, C., Zhang, Y., Li, X., Cao, H., Guo, Y., and Zhang, C. (2022). Mn-incorporated Co_3O_4 bifunctional electrocatalysts for zinc-air battery application: An experimental and DFT study. Appl. Catal. B Environ. *319*, 121909.
52. Tian, D., Denny, S.R., Li, K., Wang, H., Kattel, S., and Chen, J.G. (2021). Density functional theory studies of transition metal carbides and nitrides as electrocatalysts. Chem. Soc. Rev. *50*, 12338–12376.

STAR★METHODS

KEY RESOURCES TABLE

REAGENT or RESOURCE	SOURCE	IDENTIFIER
Software		
VASP code	VASP Software GmbH	https://www.vasp.at/
VESTA software package	JP-Minerals	https://jp-minerals.org/vesta/en/

RESOURCE AVAILABILITY

Lead contact

Further information and requests for resources should be directed to and will be fulfilled by the Lead Contact, Jia Zhou. (jiazhou@hit.edu.cn).

Materials availability

This study did not generate new unique reagents.

Data and code availability

- The published article includes all datasets generated or analyzed during this study.
- This study did not generate new code.
- Any additional information required to reanalyze the data reported in this paper is available from the lead contact upon request.

METHOD DETAILS

The DFT calculations were performed by using the Vienna Ab-initio Simulation Package (VASP).[37,38] The exchange and interactions of the electrons were described by the projector-augmented wave (PAW) method with the Perdew–Burke–Ernzerhof (PBE) functional.[39,40] The long-range dispersion correction implemented by Grimme (D3) was employed to describe the vdW interaction.[41] The spin polarization was considered in all calculations. The cut-off energy for the plane-wave basis set was assumed to be 500 eV. The Brillouin-zone integrations were sampled on a dense Γ-centered 6 × 6 × 1 k-point grid.[42] The convergence was set to 10^{-5} eV for electronic self-consistent, and 0.01 eV/Å for force. All the slabs were modelled using the 2 × 2 tetragonal transition metal chalcogenides supercell and the lattice constant along z direction of all 2D materials was fixed to 20 Å to avoid the interactions between two periodic units. The effect of aqueous solution was considered with the implicit solvation model implemented in VASPsol.[43]

The thermodynamic model of water oxidation was proposed by Nørskov, including four concerted proton-electron transfer intermediate steps. The specific mechanisms are as follows:

$$H_2O + * \rightarrow OH^* + H^+ + e^- \ \Delta G_1 \quad \text{(Equation 4)}$$

$$OH^* \rightarrow O^* + H^+ + e^- \ \Delta G_2 \quad \text{(Equation 5)}$$

$$O^* + H_2O \rightarrow OOH^* + H^+ + e^- \ \Delta G_3 \quad \text{(Equation 6)}$$

$$OOH^* \rightarrow O_2 + H^+ + e^- \ \Delta G_4 \quad \text{(Equation 7)}$$

where * represents an active site. η_{TD} was the thermodynamic overpotential introduced by Nørskov,[44] defined by $\eta_{TD} = \Delta G_{pds}/e$, where $\Delta G_{pds} = \max[\Delta G_1, \Delta G_2, \Delta G_3, \Delta G_4]$, corresponds to the free energy of the potential determination step (PDS), e is the electron charge, and 1.23 V is the oxidation potential required on the surface of an ideal catalyst for water oxidation. So, the overpotential of OER can be defined as following[7]:

$$\eta_{OER} = \max[\Delta G_1, \Delta G_2, \Delta G_3, \Delta G_4]/e - 1.23 \quad \text{(Equation 8)}$$

Under standard conditions, the overall HER can be described by the following Equation 9:

$$H^+(aq) + e^- \rightarrow 1/2H_2(g) \quad \text{(Equation 9)}$$

where the Gibbs free energy for H* adsorption ΔG_{H^*} can act as a descriptor of HER activity. In the standard hydrogen electrode, the total energy of $1/2H_2$ is equal to that of $H^+ + e^-$.[45] Therefore, the adsorption energy of hydrogen is calculated using Equation 10. According to the Sabatier principle, ΔG_{H^*} should be close to zero in order to achieve the maximum reaction rate and the highest HER catalytic activity.

$$\Delta G_{H^*} = G_{H^*} - G_* - 1/2G_{H2} \quad \text{(Equation 10)}$$

In each elementary step of the OER and HER, the free energy is calculated based on the computational hydrogen electrode model proposed by Nørskov et al.[44] Due to the maintenance of neutrality in the simulated system during successive "electrochemical steps", this method is also referred as the constant charge model (CCM).[46] However, it should be noted that in addition to CCM, the constant potential model (CPM) is considered a more accurate approach for calculating the electrocatalytic reaction process. The CPM considers the exchange of electrons with the reference system at every stage.[46–49] In comparison, the CPM requires longer computational time, and these two methods can provide the similar results.[49–52] According to the CCM, the difference of free energy between the initial state and the final state of the reactions was defined as below:

$$\Delta G = \Delta E + \Delta E_{ZPE} - T\Delta S - neU + \Delta G_{pH} \quad \text{(Equation 11)}$$

where ΔE, ΔE_{ZPE} and ΔS are the total energy changes from DFT calculations, zero-point energy and entropy difference between the reactants and the products, respectively. T is 298.15 K in our calculations. ΔG_{pH} is the correction of the free energy introduced by the difference in pH (H^+ concentration) of the solution, calculated by the formula $\Delta G_{pH} = 2.303 \times k_B \times T \times pH$, where k_B is the Boltzmann constant. pH = 0 is employed in our calculation to represent an acidic environment.

QUANTIFICATION AND STATISTICAL ANALYSIS

Calculate the variance of the adsorption energy linear relationship using Microsoft Excel.